PHOTONICS Research

Biosensing with free space whispering gallery mode microlasers

Angela Capocefalo,[1,†] Silvia Gentilini,[1,†] Lorenzo Barolo,[2] Paola Baiocco,[2] Claudio Conti,[1,3] AND Neda Ghofraniha[1,*]

[1]*Istituto dei Sistemi Complessi-CNR, UOS Università La Sapienza, I-00185 Rome, Italy*
[2]*Dipartimento di Scienze Biochimiche A. Rossi Fanelli, Università La Sapienza, I-00185 Rome, Italy*
[3]*Dipartimento di Fisica, Università La Sapienza, I-00185 Rome, Italy*
[†]*These authors contributed equally to this paper.*
Corresponding author: neda.ghofraniha@cnr.it

Highly accurate biosensors for few or single molecule detection play a central role in numerous key fields, such as healthcare and environmental monitoring. In the last decade, laser biosensors have been investigated as proofs of concept, and several technologies have been proposed. We here propose a demonstration of polymeric whispering gallery microlasers as biosensors for detecting small amounts of proteins, down to 400 pg. They have the advantage of working in free space without any need for waveguiding for input excitation or output signal detection. The photonic microsensors can be easily patterned on microscope slides and operate in air and solution. We estimate the limit of detection up to 148 nm/RIU for three different protein dispersions. In addition, the sensing ability of passive spherical resonators in the presence of dielectric nanoparticles that mimic proteins is described by massive *ab initio* numerical simulations. © 2023 Chinese Laser Press

1. INTRODUCTION

Light in a dielectric hollow cavity of micrometric size is trapped on its surface in so-called whispering gallery modes (WGMs). For high quality-factors Q, the enhancing interaction with the dielectric environment makes WGM resonators sensitive to infinitesimal variations of the surrounding refractive index, leading to a measurable shift of the resonance wavelength [1,2]. In the last two decades, ultrahigh Q passive microcavities have been used for label-free single molecule detection by employing lithographed silica microresonators with very high sensitivity. Highly diluted samples, such as 10^{-18} M (1 M = 1 mol/L) of interleukin-2 and 1 pM of influenza-A virus, have been successfully detected by using tapered fiber and interferometric techniques [3,4].

Active cavities that support stimulated emission modulated by WGM resonances can be obtained by including a gain medium in the dielectric cavity. The first WGM laser was made from a highly polished crystalline calcium fluoride (CaF_2) sphere of 1–2 mm diameter, and the rare-earth samarium ion (Sm^{2+}) was used as the optical gain dopant [5]. Since then, lasing has been demonstrated in many different spherical WGM cavity geometries [6,7] and others [8], such as triangular nanoplatelets [9], ZnO hexagonal and dodecagonal microrods, nanonails, and microgoblets [10,11].

During the last few years, promising applications of WGM microlasers in biosensing have been reported, such as lasing within living cells [12,13], monitoring contractility in cardiac tissue [14], detection of electrostatic changes induced by molecules at biointerfaces [15], label-free detection of single virus particles [16], and advancement of *in vivo* sensing [17].

The use of WGM microlasers for chemical and biological sensing can offer assets that are often not easily accessed on other optical WGM sensors [18]. Indeed, the advantages of using microlaser emission compared to the transmission of silica microparticles measured by a fiber tapered technique, of more widespread use, are the ease in assembling the compact and versatile optical setup due to free space detection without any need of fine wave guiding [19,20], the possibility of exciting a high number of microresonators with good statistics of the measurements, and the benefit of using materials other than silica without resorting to lithographic techniques that require the use of clean rooms and specific infrastructures.

In vivo sensing with WGM microlasers is facilitated by direct visualization of the emission of relatively bright laser light at frequencies that are spectrally well separated from the frequency of the free space excitation beam.

Furthermore, WGM microlasers offer potentially very high detection sensitivity for molecules due to the narrow linewidth

of the laser lines. The detection of a very low concentration of biomolecules becomes possible if these spectral WGM shifts are resolved. Besides line shifting, other interesting WGM sensing modalities have been reported [16,21–24].

Biosensors with WGM laser activity have been realized by using liquid droplets for the detection of inoculated bacteria [25], intracellular investigation [17], and real time enzymatic reaction [15]. In addition, optofluidic lasers have been fabricated for DNA and virus sensing as well as enzymatic reaction catalysis. In these sensors, WGMs are activated directly on the walls of the channels where biofluids flow, and biomolecules are detected [26,27].

The limits of these biosensors are the restricted rigidity and stability of the droplets and the difficulties of doing surface treatments for specific detection [28–31]. To this aim, using polymeric microlasers operating in both air and solution is essential and still being explored with a few examples reported. These have been inoculated in cells for the follow-up of intracellular activity and cell tagging and tracking [12]. Different solid polymeric microlasers have been obtained and characterized [32,33], but none has shown sensitivity to the external presence of biomolecules indispensable for immunoassays and sensing devices.

Here we report on the realization and characterization of laser-based biosensors made of single or arrays of dyed polymeric spheres patterned on glass substrates. They operate in both air and solution and present evident emission line shifts once covered with a drop of protein solution. We obtain a limit of detection (LOD) of 0.38 ng for lysozyme protein in air. This limit is the lowest for bare spheres with non-specific protein bindings. We test the microlaser biosensor on three different protein suspensions obtaining a sensitivity of 148 nm/RIU for tau protein suspension. The results are achieved by using an experimental setup that allows to map emission spectra along the equatorial sections of the lasing spheres. This way, it is possible to perform averages of spectral shifts over different probe points and increase the accuracy of the results. To have good statistics and significant data, we repeat the same operation on arrays of about 30 microspheres, and we record and analyze emission spectra by carrying out automated scanning of the assays. Our experimental results open the way to the development of optical devices for specific and highly sensitive detection and potentially optimized to be used as photonic immunoassays and early-stage disease biosensors.

In addition, we describe an advanced numerical investigation of light localization on the surface of a WGM spherical cavity in both time and space. We perform three-dimensional finite difference time domain (3D-FDTD) simulations to show numerically significant spectral line shifts in the presence of nanoparticles on the microsphere surface.

This investigation is relevant in support of experimental procedures and fine spectral analysis.

2. METHODS

A. Experimental Setup and Characterization

In this investigation, we show and analyze the performance of microlaser biosensors made of fluorescent polystyrene microspheres. The dry-dyed polystyrene microspheres (Fluoro-Max Dry) with a nominal diameter of 30 μm were purchased from Thermo Scientific. The refractive index is $n = 1.59$ at 589 nm (25°C). The microspheres are dissolved in MilliQ water and conveniently diluted before deposition.

For sample deposition, a grid pattern of squares is realized on the glass slides using a diamond tip glass cutter, and then the slides are functionalized by soaking them in a 3% ethanol solution of (3-aminopropyl)triethoxysilane (APTES, Sigma Aldrich) for 3 h. Afterwards, the glass slides are rinsed with ethanol and water and left to dry. The glass slides are functionalized with APTES to fix the microsphere to the substrate and avoid their movement during experiments. Subsequently, 5 μL of the microsphere solution is incubated in each square until the water is completely evaporated.

This way, we obtain approximately one microsphere per square. We then use a homemade micromanipulator made of an atomic force microscope cantilever properly mounted on motorized translation stages. By using controlled movements of the translators, we are able to adjust microsphere positions and produce arrays of 30 microspheres per slide. A sketch of the so-obtained sample is reported in Fig. 1(a).

The microspheres are excited by a *Q*-switched Nd:YAG pulsed laser operating at 532 nm, with 4 ns pulse duration and 10 Hz repetition rate. The input energy of the laser is modulated by a variable neutral density filter mounted onto a motorized stage. The pump light is then split in half through a beam splitter, and the reflected part is measured by an energy meter to monitor the pump energy variations. The transmitted beam is focalized on the sample with an objective with a spot size of ∼50 μm to excite the whole microsphere as proposed previously for similar microlasers [12–14,17]. The emission from the single microspheres is 30× magnified by an objective with NA = 0.4 and filtered by a notch filter to remove residual pump light [34,35]. The filtered light is then split on a Retiga R1 charge-coupled device (CCD) camera for fluorescence imaging and on an optical fiber, with 50 μm core diameter, connected to a Horiba-Jobin Yvon spectrometer that uses an asymmetric Czerny–Turner optical path with 140 mm focal length. A diffraction grating with density of 1800 grooves/mm and blaze 500 nm is used, and the spectrograph is coupled to a Symphony cooled CCD system with 13.5 μm pixel size. In our experiments, the instrumental spectral resolution is 0.11 nm. The fiber is mounted on motorized stages moving in two perpendicular directions with 25 μm step size, which corresponds to about 1 μm on the sample plane. A fine calibration is performed to have a precise correspondence between the selected CCD pixels and the fiber position. This way, we can scan and record the lasing emission [36] from planar sections of the microlasers as visualized on the camera. A sketch of the setup is reported in Fig. 1(a). With this setup, excitation and detection are decoupled allowing to do scans of the emission on the plane that is imaged on the CCD.

A representative fluorescence image of a single microlaser is illustrated in Fig. 1(b), where a higher emission intensity at the edges of the sphere is evident.

The lasing emission spectrum of a single microlaser immersed in water is depicted in Fig. 1(c). The observed multi-lasing lines correspond to the excited WGMs sustained
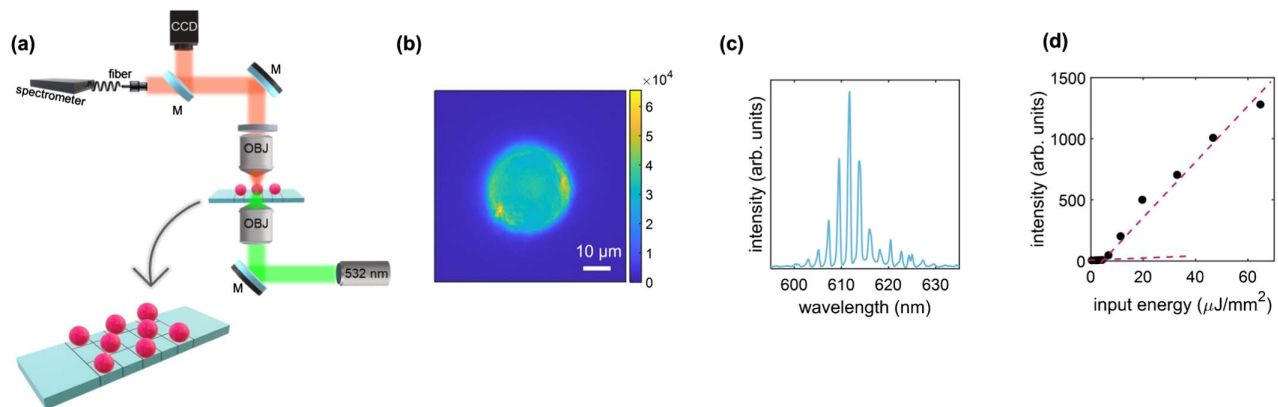
Fig. 1. Optical characterization of lasing polystyrene microspheres. (a) Sketch of the optical setup and of the sample employed in the experiment. The polystyrene microspheres are deposited onto a microscope slide with grids previously functionalized with APTES. The laser light is focused on the sample by an objective with a spot size of ∼50 μm. The light emitted by the sample is collected by a second objective and then is split on a charge-coupled device camera for fluorescence imaging and on an optical fiber connected to a spectrometer. (b) Fluorescence image of a single polystyrene microsphere. (c) Emission spectra of a microlaser in water; WGMs are evident. (d) Spectral intensity versus input pumping showing the threshold between spontaneous and stimulated emission estimated at about 7 μJ/mm².

by the fluorescence band. The free spectral range (FSR) is about 2.5 nm, which is consistent with the expected value $\Delta\lambda = \lambda^2/2\pi nR$, where $R = 15$ μm is the radius of the sphere and $n = 1.59$ its refractive index. Mode number is estimated to be ∼238 and 239 [37].

In Fig. 1(d), the emission intensity versus increasing energy density presents a rapid growth after the threshold between spontaneous and stimulated emission at about 7 μJ/mm². This value is obtained from the intersection of the two linear fits. For these measurements, a spot size with 0.6 mm diameter is used.

In this work, we use a pumping laser energy density of about 17 μJ/mm², which is well above the laser threshold; the system has sufficient gain to activate laser action with many equally spaced modes.

We use microspheres with a diameter of 30 μm to have an appreciable FSR of about 2.5 nm in relation to the instrumental spectral resolution of 0.11 nm. This choice allows the separation of individual resonances indispensable for line shifting examination. In addition, the selected size guarantees a suitable amount of gain inside the resonators with consequent low laser thresholds.

B. Tau Protein Preparation

Tau protein was designed from 244 to 376 amino acids and is referred to as the K18 domain, which contains four microtubule-binding repeats (MTBRs). K18 was expressed in an *E. coli* BL-21DE-3 strain and purified from a high-density cell paste (Genscript Biotech Corporation) as described elsewhere [38]. The purified fractions were pooled and dialyzed in a phosphate-buffered saline (PBS) pH 7.4 and then concentrated using 3 kDa cutoff protein centrifugal filters. Separation of the monomeric from higher oligomers was performed by size exclusion chromatography applying protein samples in PBS on a Hiload 26-600 Superdex 75 equilibrated in the same buffer. The concentration of tau (5 mg/mL) was determined by UV absorption at 270 nm using an extinction coefficient of $\epsilon = 1490$ M⁻¹ cm⁻¹ with a Jasco V-750 (Jasco Corporation, Tokyo, Japan).

C. Numerical Simulations

To mimic the sensing performance of microresonators, we use an advanced 3D-FDTD code that reproduces electromagnetic behavior by solving the Maxwell equations with a first principle approach based on the FDTD algorithm. The Maxwell equations are discretized on faces and sides of a cubic Yee grid [39]. We used a technique developed by the authors in previous works [40,41]. Standard leapfrogging is used as the time marching algorithm, and a uniaxial perfectly matched layer (UPML) is employed to absorb outgoing waves. The code is finally parallelized within the message-passing interface (MPI) [42]. We run the code on a large-scale computational facility where a typical run requires about 5 h of calculation using about 1500 processors.

3. RESULTS AND DISCUSSION

A. Spherical Microlasers for Biosensing

For biosensing tests on liquid samples, we first soak the array of 30 microlasers, previously deposited on a glass slide, in water and take the emission spectra from different points of all spheres by automatized scanning. After water evaporation, we add a 5 μL drop of protein solution onto each microlaser, as sketched in Fig. 2(a).

Then, we measure emission spectra from the same points of the spheres considered for the water signal detection used as a reference. This procedure is necessary because the spectral configuration of the WGM and, thus, the emission spectra are dependent on the position of the probe point on the sphere. For this crucial issue, to compare the emission spectra, we detect them from the exactly same point on the edge of the same microsphere in all measurements. We repeat this operation on the array.

We take spectra from different sampling points on the edge of each sphere because the emission spectra might be slightly diverse as shown previously [17]. We estimate peak position variations of 0.01 nm for bare microspheres. Data are reported
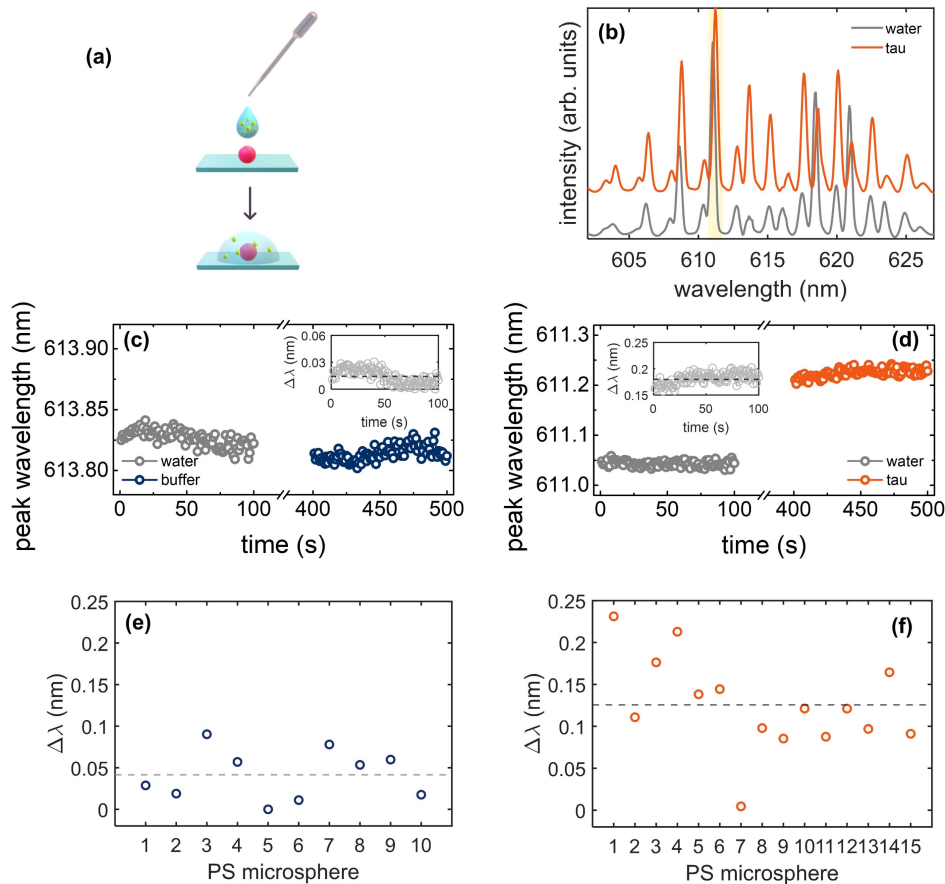
Fig. 2. Analysis of the wavelength shift of the lasing emission peaks of a single polystyrene microsphere in liquid induced by the absorption of tau proteins. (a) Sketch of the experiment. A drop of protein solution is deposited onto a polystyrene microsphere, and emission spectra are acquired on the soaked microsphere. (b) Emission spectra of a microsphere immersed in water (gray) and in tau protein (orange) suspension. (c), (d) Time evolution of the central emission wavelength, obtained by peak fitting, of a selected lasing peak (highlighted in yellow in the spectra in the top panel) for PBS buffer [blue (c)] and tau protein [orange (d)]. Time interval between two depositions is about 5 min. In the insets, the trend of the corresponding wavelength shift $\Delta\lambda$ is reported. (e), (f) Values of the wavelength shifts $\Delta\lambda$ obtained for different microspheres for PBS buffer (e) and tau proteins (f). The dashed lines indicate the average value of $\Delta\lambda$.

in Appendix A, Fig. 5. Even though this variation is well below the instrumental resolution, we use the spectral scanning technique to have good statistics and to validate the small peak shifts measured in the presence of proteins.

The evaluation of the biosensing capability of the microlasers is performed by employing the clinically relevant tau protein. It is a very flexible and highly soluble protein that belongs to the microtubule-associated protein family. Tau proteins have been identified for Alzheimer's disease biomarkers [38,43]. In Fig. 2(b), we report representative spectra for water and aqueous solution of tau protein. Small peak redshifts of the water–protein solution curves with respect to the pure water ones are observed.

To have a quantitative and significant estimation of the small resonance shifts, we monitor the temporal evolution of the detected spectra as proposed in Refs. [3,14,44]. Lasing emission spectra as a function of time are acquired from several points of the array as described above. From each spectrum, we select the three to four peaks with the highest intensity and measure the central wavelength position of each of them in time by fitting the selected peak to a Gaussian function [14].

Since the protein is dissolved in PBS buffer solution, we first evaluate the effect of the buffer on the microresonator by comparing the position of the selected lasing peak with respect to water as reported in Fig. 2(c). For each sampling point, the temporal average of the resonance wavelengths of water (reference) and buffer solution is calculated. Then the resonance shift $\Delta\lambda$ for each peak is obtained as reported in the inset of Fig. 2(c). We do not observe significant variations in the measured peak wavelength of the microlaser in the buffer solution with respect to water. For this reason and considering that the PBS buffer evaporation leads to the formation of salt crystals that hinder the lasing of the microspheres, we chose water as a reference.

As evidenced in Fig. 2(d), the measured peak wavelength corresponding to the tau protein solution is significantly different from that obtained for the reference. We estimate the average over all the measured $\Delta\lambda$ for different microspheres for both buffer and protein solution, as reported in Figs. 2(e) and 2(f). We obtain an average $\Delta\lambda$ of 0.02 ± 0.05 nm for PBS buffer and of 0.13 ± 0.01 nm for tau proteins. The measured $\Delta\lambda$ for PBS buffer is not significant within the instrumental error defined by the spectral resolution. The values measured for tau

proteins, instead, are above the spectral resolution, pointing out the reliability of the proposed strategy for revealing the presence of the protein in the solution.

From the line shifts, we can estimate the sensitivity $\Delta\lambda/\Delta n$ of the microlaser in liquid. The refractive index variation Δn, expressed in RIUs, is evaluated as the difference between the effective refractive index n_{eff} of the protein solution and the n_w of water. Specifically, the refractive index of the protein solution is calculated from the volume fraction of the protein according to the Lorentz–Lorenz relation for liquid mixtures [45], considering $n_{\mathrm{tau}} = 1.602$ [46] and $n_w = 1.33$. The calculated value for tau protein is $n_{\mathrm{eff}} = 1.3308$ at the concentration used in the experiment. From the corresponding small variations $\Delta n_{\mathrm{tau}} = 0.0008$, we obtain a sensitivity value of 148 nm/RIU. Considering that we do not observe any significant wavelength shift in the case of PBS buffer with respect to water, the adsorption of proteins on the microsphere surface could provide an enhanced wavelength shift of the mode. To extend the characterization of the proposed system, we perform the experiment on liquid samples of other protein solutions, as reported in Appendix B. We may notice that the estimated wavelength shifts for all protein dispersions are comparable, giving the highest sensitivity obtainable with this biosensing technique and its robustness. The different sensitivities obtained for the three different proteins can be ascribed to a different adhesion degree of the proteins on the microlaser surface.

In the following, we investigate the sensing capabilities of the laser biosensor in air. We present this second strategy because in the absence of a liquid solution and in air, the mismatch of the refractive index at the interface of the microspheres is higher. This allows to gain a much lower LOD for those cases where the presence of the solvent is not relevant.

To do so, we perform multiple depositions of 3 μL droplets of lysozyme aqueous solution with 0.3 μg/mL concentration, and we leave the water to evaporate as represented in the sketch of Fig. 3(a). We acquire emission spectra on the dried

microsphere prior to the subsequent deposition. A selected single lasing peak at the varying protein concentration is reported in Fig. 3(b) together with the spectrum of the microsphere measured in air as blank. From Fig. 3(b), a progressive shift of the lasing peak with increasing lysozyme concentration is clearly evident. The spectral shift $\Delta\lambda$, corresponding to the difference between the central wavelength of the lasing peak in the presence of protein molecules and the reference emission of the bare microsphere, obtained by peak fitting, is reported in Fig. 3(c) as a function of lysozyme protein mass M_p in nanograms.

We perform the same operation on the three to four most intense resonances of the spectra from 30 spheres; the values in Fig. 3(c) are the calculated averages, and error bars correspond to the standard deviations.

The growth follows the typical saturation model (also named Monod's equation)

$$\Delta\lambda = \frac{aM_p}{b + M_p}, \tag{1}$$

represented by the fitting dashed curve in Fig. 3(c) and with a and b fitting parameters, while the low concentration region shows a linear regime (red line). We evaluate the LOD of the WGM microspheres from this linear region of the trend. In detail, we determine the LOD from the slope s obtained by the linear fitting according to the relation $\mathrm{LOD} = \frac{3\sigma}{s}$, where σ is the standard deviation of the blank [47]. Here we consider $\sigma = 0.014$ nm, as calculated from the data reported in the inset of Fig. 2(c). Therefore, we obtain an LOD equal to 0.38 ng for the microlaser operating in air.

This calculation is performed assuming that all proteins in the solution are adsorbed to the microsphere. Actually, only a fraction of them will be in contact with the microlaser, and the rest will settle on the glass slide. Therefore, here we provide an overestimation of the LOD that is expected even an order of magnitude lower if we consider the ratio between droplet and microsphere diameters. The estimated LOD is the minimum
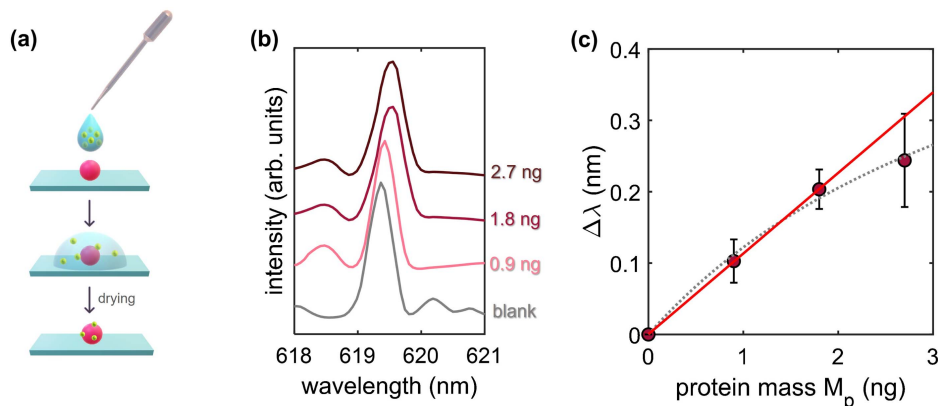

Fig. 3. Analysis of the wavelength shift of the lasing emission peaks of a single polystyrene microsphere due to multiple depositions of lysozyme solution. (a) Sketch of the experiment. A drop of lysozyme solution is deposited onto a polystyrene microsphere and left to dry. The procedure is repeated three times. (b) Zoom on a selected lasing peak of the microsphere emission spectra at varying lysozyme amounts compared with the emission spectra of the bare microsphere (gray). (c) Average wavelength shifts of selected lasing peaks as a function of the lysozyme protein mass M_p. The averages are calculated on the three to four most intense resonances of whole spectra from different points of 30 spheres. The dashed gray curve represents the saturation growth fitting curve following Eq. (1), and the red line indicates the linear fit in the low concentration regime to extrapolate the limit of detection.

amount of biomolecules in a solution that can be detected by the microlaser sensor after solvent evaporation.

The estimated LOD is the best obtainable with bare microlasers. For better performance, further strategies are required. Specific surface chemical binding would be useful to catch the few biomolecules present in solution. Plasmonic nanoparticles coupled to optical WGMs would increase the sensitivity of the proposed polymeric microlasers. Label-free single molecule detection has been demonstrated by using metallic nanoparticles chemically attached to the surface of passive microresonators to obtain hot spots with a more intense and localized electromagnetic field. Biomolecules are then chemically attracted by these hotspots, and due to this powerful technique, single DNA molecules, single atomic ions, and enzyme conformational dynamics have been reported [44,48,49]. A different spectral analysis going beyond line shift measurements and taking into account the mutual intensity of the modes, their splitting, and fine variations could be a breakthrough in the use of microlasers as biosensors.

B. 3D-FDTD Simulations of Whispering Gallery Sensing

To provide a qualitative description of the experiments, we perform a numerical experiment by using the FDTD method [39]. We excite WGM on the surface of a 3 μm diameter sphere of polystyrene with refractive index $n_p = 1.6$ in air. To study the detection capability of the WGM sensor, we surround the microsphere with a uniform random distribution of 10 nm diameter dielectric spheres with refractive index $n_{NP} = 1.5$. The size and refractive index of the nanoparticles are chosen to mimic biomolecules in the experiments.

In this investigation, we scale the size of the microresonators by a factor of 10 compared to that of the experiments because reproducing the particle/wavelength ratio of the experiments would require a spatial grid whose computational cost is not affordable for this study. Such geometrical change affects the features of the spectra in terms of spacing and quality factor of the WGMs. However, the simulations can still have the ability to sense nanoscopic refractive index variation on the surface and the light coupling, which is a disruptive element of our experimental approach.

For the simulations, we laterally hit the surface of the microsphere with a Gaussian TEM$_{00}$ linearly y-polarized input pulse, with $1/e$ field-waist $w_0 = 0.2$ μm. The input pulse temporal profile is also Gaussian with a duration $t_0 = 100$ fs and carrier wavelength $\lambda = 532$ nm. We use a short pulsed input to have a wider spectral content and facilitate the excitation of WGM resembling the experiments.

In Figs. 4(a) and 4(b), we illustrate the bare microsphere and the microsphere surrounded by nanoparticles together with snapshots of the corresponding spatial profiles of the electric field E_y in the x–y (bottom), y–z (right), and x–z (left) obtained by slicing the sphere in the middle planes. The spatial maps of E_y display the characteristic profile of the WGM, which is not perturbed by the presence of the nanoparticles. The presence of the latter is unveiled by spectral line shifting as demonstrated by the spectra reported in Figs. 4(c) and 4(d).

Details on spectral calculation are reported in Appendix C. Here we evidence that the FSR calculated as the spacing
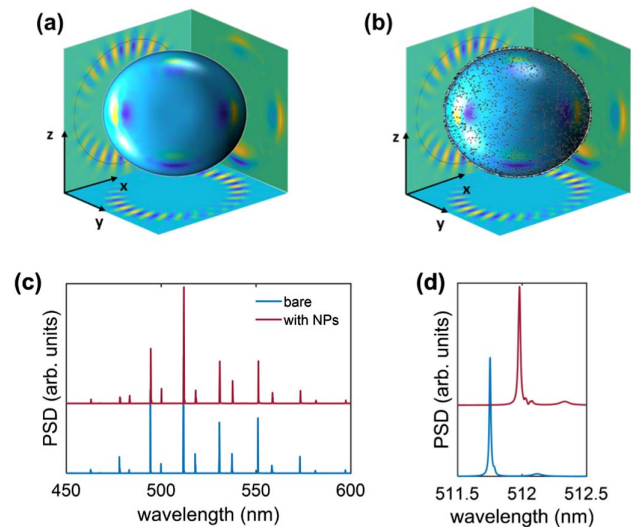

Fig. 4. 3D-FDTD numerical simulations. (a) Illuminated bare microsphere and (b) microsphere surrounded by nanoparticles with a snapshot of the x–y (bottom), y–z (right), and x–z (left) spatial profiles of the electric field obtained slicing the sphere in the middle planes. (c) Normalized spectrum of $E_y(t)$ calculated by means of the Fourier transform for the bare microsphere (blue) and for the microsphere surrounded by nanoparticles (red) at volume fraction $\phi = 0.1$. (d) Zoom on the most intense peak of the spectra, showing the redshift $\Delta\lambda = 0.25$ nm in the presence of nanoparticles.

between two adjacent peaks results in $\Delta\lambda \simeq 20$ nm, which is in excellent agreement with the theoretical FSR [37]: $\Delta\lambda = \lambda^2/2\pi nR$, where R is the radius of the sphere, and n its refractive index.

In Fig. 4(d), a zoom on one peak demonstrates a line shift $\Delta\lambda = 0.25$ nm for nanoparticle volume fraction $\phi = 0.1$.

Variations of wavelength shift versus the volume fraction of the nanoparticles adsorbed to the microsphere are reported in Appendix C.

4. CONCLUSION

In conclusion, here we propose and study polymeric microlasers as efficient biosensors. We realize arrays of dyed microspheres, and we detect the emission spectra from several points on each sphere and from different spheres. Due to an automated optical setup, the advantage of using free space detection, and by monitoring the spectral variations in time, we are able to scan the emission over hundreds of points and accurately calculate spectral shifts with good statistics. This procedure mitigates the low-resolution limit of spectrometers and allows to obtain an LOD of 0.38 ng for lysozyme protein in air and a sensitivity $\Delta\lambda/\Delta n$ with respect to RIU variations of 148 nm/RIU for tau protein, which is one of the major hallmarks of Alzheimer's disease.

We also develop and perform 3D-FDTD numerical investigation to simulate the response of microresonators to incident laser radiation and light trapping resulting in whispering gallery resonances. We obtain numerical spectra with picometer wavelength resolution, and we report evident resonance shifts when dielectric nanoparticles are added to the surface. This

way, we simulate a true biosensor, and our findings are helpful to design and realize sensing devices based on WGM cavities.

With this investigation, we provide a proof of concept of high-sensitivity detection of biomolecules in both dried and wet conditions by exploiting the advantage of a free space setup. Our results open the way to the fabrication of portable immunoassays for specific and accurate sensing. More importantly,

microlasers can be easily visualized and used both for tagging cells and monitoring their activity in time.

APPENDIX A: EMISSION SPECTRAL SCANNING

We report in Fig. 5 different emission spectra taken at different points on the edge of a bare microlaser. We evaluate the peak position by using the peak fitting procedure as described in the
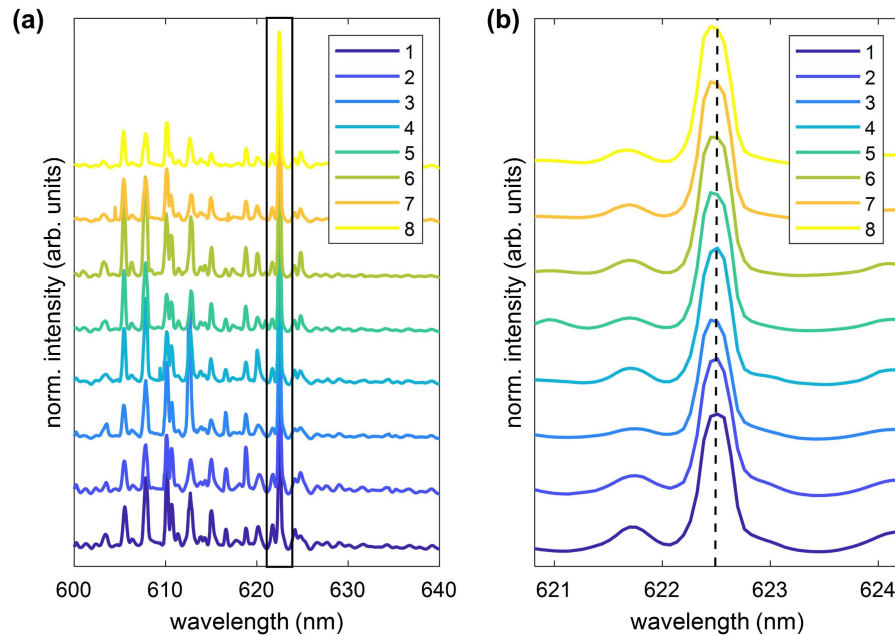

Fig. 5. (a) Spectra taken at different points on the edge of a microlaser and (b) zoom on one peak.
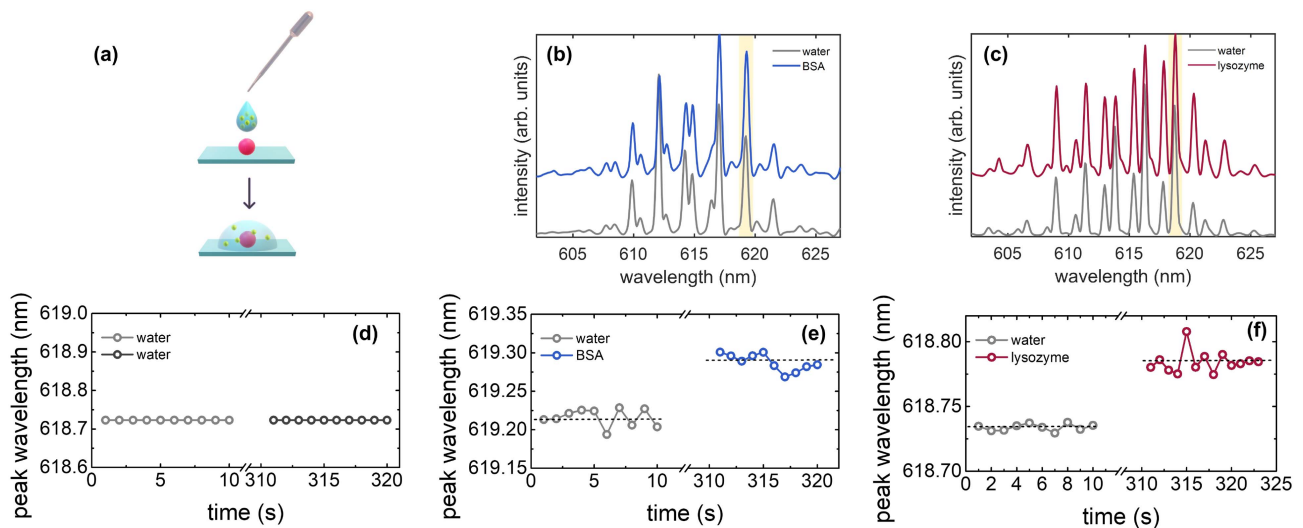

Fig. 6. Analysis of the wavelength shift of the lasing emission peaks of a single polystyrene microsphere in liquid induced by the absorption of BSA and lysozyme proteins. (a) Sketch of the experiment. A drop of protein solution is deposited onto a polystyrene microsphere, and emission spectra are acquired on the soaked microsphere. (b), (c) Emission spectra of two different microspheres immersed in water (gray) and in BSA [blue (b)] and lysozyme [red (c)] suspensions. The volume fractions of the protein dispersions are $\phi_{BSA} = 0.016$ and $\phi_{lysozyme} = 0.007$. (d)–(f) Time evolution of the central emission wavelength of a selected lasing peak (highlighted in yellow in the spectra in the top panels) for BSA [blue (e)] and lysozyme [red (f)]. In (d), peak positions of two different water drops are reported. The dashed lines indicate average values. Time interval between two depositions is about 5 min.

paper, and we find an average variation of $\Delta\lambda = 0.01$ nm. This value is well below the instrumental resolution and validates the results on sensing for protein suspensions.

APPENDIX B: BIOSENSING OF BSA AND LYSOZYME PROTEINS

In Figs. 6(b) and 6(c), we report representative spectra for water and two different aqueous protein solutions, bovine serum albumin (BSA) and lysozyme at 20 mg/mL and 10 mg/mL concentrations, respectively, corresponding to volume fractions $\phi_{BSA} = 0.016$ and $\phi_{lysozyme} = 0.007$.

Peak positions are estimated by a peak fitting procedure as discussed in the paper for tau protein. The temporal evolution of one peak for pure solvent and protein suspension is reported in Figs. 6(e) and 6(f). We estimate the average over all the measured $\Delta\lambda$ for each protein suspension with final results of 0.09 ± 0.01 nm for BSA and 0.12 ± 0.03 nm for lysozyme. The averages are made over different sampling positions (four points per sphere for 30 spheres) and three to four peaks in each spectrum. In Fig. 6(d), we show wavelength position evolution

for two water depositions, demonstrating that the observed line shifts are due to the presence of proteins.

We can estimate the sensitivity $\Delta\lambda/\Delta n$ of the microlaser in liquid from the line shifts. The refractive index variation Δn, expressed in RIUs, is evaluated as the difference between the effective refractive index n_{eff} of the protein solution and that n_w of water, as described in the main text. We here consider $n_{BSA} = 1.599$, $n_{lysozyme} = 1.620$ [50], and $n_w = 1.33$. The so calculated values are $n_{eff} = 1.3338$ for BSA–water and $n_{eff} = 1.3317$ for lysozyme–water dispersions at the concentrations used. From the corresponding small variations $\Delta n_{BSA} = 0.0038$ and $\Delta n_{lysozyme} = 0.0018$, we, therefore, obtain sensitivity values of 20.9 nm/RIU and 65.6 nm/RIU in the case of BSA and lysozyme, respectively.

APPENDIX C: 3D-FDTD SIMULATIONS OF WHISPERING GALLERY SENSING

The result of a simulation for a bare microsphere is reported in Fig. 7. In Fig. 7(a), a snapshot of the xy spatial profile of the electric field in the middle plane of the sphere is illustrated. In
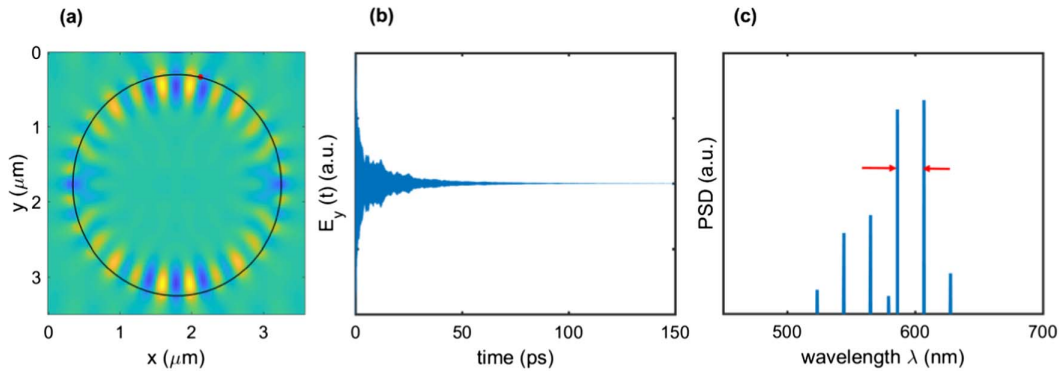

Fig. 7. 3D-FDTD numerical simulations. (a) Snapshot of the xy spatial profile of the electric field in the middle plane of the sphere. (b) Y-component of the electric field, $E_y(t)$ evolution collected in a point on the surface of the sphere [red bullet in (a)]. (c) Normalized spectrum of $E_y(t)$ calculated by means of the Fourier transform.
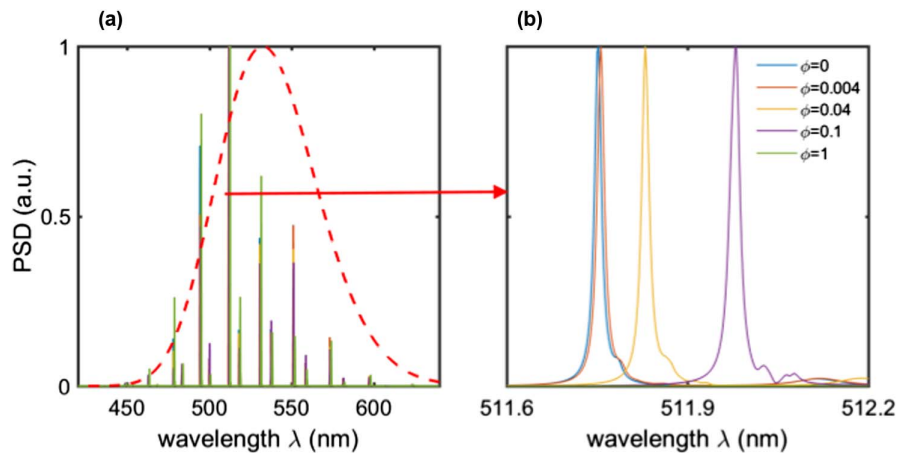

Fig. 8. Numerical FDTD sensing. (a) Superimposed spectra of $E_y(t)$ as obtained for five different volume fractions ϕ of dielectric nanoparticles randomly distributed on the sphere surface. The red dashed curve indicates the spectral content of the short pulsed input excitation. (b) Zoom on the central peak at varying nanoparticle volume fractions.

Fig. 7(b), we report the temporal profile $E_y(t)$ as collected on the surface of the microsphere at the point indicated by the red bullet drawn in Fig. 7(a). The 150 ps collected signal $E_y(t)$ is then Fourier transformed to obtain the spectrum reported in Fig. 7(c). This latter displays the fingerprint of the WGMs.

To provide a qualitative description of the sensing properties of WGM microspheres, we consider four different volume fractions $\phi = [0.004, 0.04, 0.1, 1]$, where $\phi = 1$ means considering a 10 nm thick coating covering the microsphere.

For the analysis, we compare the spectra calculated by the collected $E_y(t)$ at the same point of the microsphere for different volume fractions ϕ of the nanoparticles distributed on the surface. The spectra calculated are reported in Fig. 8(a). In Fig. 8(b), the zoom on the central peak in (a) reveals an increasing shift with respect to the peak of the spectrum of the bare sphere, λ_0.

Disclosures. The authors declare no competing interests.

Data Availability. Data underlying the results presented in this paper are not publicly available at this time but may be obtained from the authors upon reasonable request.

REFERENCES

1. L. Cai, J. Pan, Y. Zhao, J. Wang, and S. Xiao, "Whispering gallery mode optical microresonators: structures and sensing applications," Phys. Status Solidi A **217**, 1900825 (2020).
2. E. Kim, M. D. Baaske, and F. Vollmer, "Towards next-generation label-free biosensors: recent advances in whispering gallery mode sensors," Lab Chip **17**, 1190–1205 (2017).
3. T. Lu, H. Lee, T. Chen, S. Herchak, J.-H. Kim, S. E. Fraser, R. C. Flagan, and K. Vahala, "High sensitivity nanoparticle detection using optical microcavities," Proc. Natl. Acad. Sci. USA **108**, 5976–5979 (2011).
4. A. M. Armani, R. P. Kulkarni, S. E. Fraser, R. C. Flagan, and K. J. Vahala, "Label-free, single-molecule detection with optical microcavities," Science **317**, 783–787 (2007).
5. C. G. B. Garrett, W. Kaiser, and W. L. Bond, "Stimulated emission into optical whispering modes of spheres," Phys. Rev. **124**, 1807–1809 (1961).
6. R. E. Benner, P. W. Barber, J. F. Owen, and R. K. Chang, "Observation of structure resonances in the fluorescence spectra from microspheres," Phys. Rev. Lett. **44**, 475–478 (1980).
7. S. Nizamoglu, M. C. Gather, and S. H. Yun, "All-biomaterial laser using vitamin and biopolymers," Adv. Mater. **25**, 5943–5947 (2013).

8. T. Reynolds, N. Riesen, A. Meldrum, X. Fan, J. M. M. Hall, T. M. Monro, and A. Francoi, "Fluorescent and lasing whispering gallery mode microresonators for sensing applications," Laser Photon. Rev. **11**, 1600265 (2020).
9. G. Li, T. Che, X. Ji, S. Liu, Y. Hao, Y. Cui, and S. Liu, "Record-low-threshold lasers based on atomically smooth triangular nanoplatelet perovskite," Adv. Funct. Mater. **29**, 1805553 (2019).
10. D. Wang, H. W. Seo, C.-C. Tin, M. J. Bozack, J. R. Williams, M. Park, and Y. Tzeng, "Lasing in whispering gallery mode in ZnO nanonails," J. Appl. Phys. **99**, 093112 (2006).
11. T. Wienhold, S. Kraemmer, S. F. Wondimu, T. Siegle, U. Bog, U. Weinzierl, S. Schmidt, H. Becker, H. Kalt, T. Mappes, S. Koeber, and C. Koos, "All-polymer photonic sensing platform based on whispering-gallery mode microgoblet lasers," Lab Chip **15**, 3800–3806 (2015).
12. M. Schubert, A. Steude, P. Liehm, N. M. Kronenberg, M. Karl, E. C. Campbell, S. J. Powis, and M. C. Gather, "Lasing within live cells containing intracellular optical microresonators for barcode-type cell tagging and tracking," Nano Lett. **15**, 5647–5652 (2015).
13. V. D. Ta, S. Caixeiro, F. M. Fernandes, and R. Sapienza, "Microsphere solid-state biolasers," Adv. Opt. Mater. **5**, 1601022 (2017).
14. M. Schubert, L. Woolfson, I. R. Barnard, A. M. Dorward, B. Casement, A. Morton, G. B. Robertson, P. L. Appleton, G. B. Miles, C. S. Tucker, S. J. Pitt, and M. C. Gather, "Monitoring contractility in cardiac tissue with cellular resolution using biointegrated microlasers," Nat. Photonics **14**, 452–458 (2020).
15. Z. Wang, Y. Zhang, X. Gong, Z. Yuan, S. Feng, T. Xu, T. Liu, and Y.-C. Chen, "Bio-electrostatic sensitive droplet lasers for molecular detection," Nanoscale Adv. **2**, 2713–2719 (2020).
16. H. Lina, O. S. Kaya, Z. Jiangang, K. Woosung, and Y. Lan, "Detecting single viruses and nanoparticles using whispering gallery microlasers," Nat. Nanotechnol. **6**, 428–432 (2011).
17. M. Humar and S. H. Yun, "Intracellular microlasers," Nat. Photonics **9**, 572–576 (2015).
18. N. Toropov, G. Cabello, M. P. Serrano, R. R. Gutha, M. Rafti, and F. Vollmer, "Review of biosensing with whispering-gallery mode lasers," Light Sci. Appl. **10**, 1 (2021).
19. D. D'Ambrosio, M. Capezzuto, S. Avino, P. Malara, A. Giorgini, P. D. Natale, and G. Gagliardi, "Light pressure in droplet micro-resonators excited by free-space scattering," Opt. Lett. **46**, 3111–3114 (2021).
20. D. D'Ambrosio, X. Zambrana-Puyalto, M. Capezzuto, A. Giorgini, P. Malara, S. Avino, and G. Gagliardi, "Angular-momentum coupling of optical whispering-gallery modes to liquid droplet microresonators," Phys. Rev. A **104**, 043504 (2021).
21. M. Himmelhaus and A. Francois, "In-vitro sensing of biomechanical forces in live cells by a whispering gallery mode biosensor," Biosens. Bioelectron. **25**, 418–427 (2009).
22. W. Chen, J. Zhang, B. Peng, Ş. K. Özdemir, X. Fan, and L. Yang, "Parity-time-symmetric whispering-gallery mode nanoparticle sensor," Photon. Res. **6**, A23–A30 (2018).
23. D. S. Weiss, V. Sandoghdar, J. Hare, V. Lefèvre-Seguin, J.-M. Raimond, and S. Haroche, "Splitting of high-Q Mie modes induced by light backscattering in silica microspheres," Opt. Lett. **20**, 1835–1837 (1995).
24. Z. Yuan, Z. Wang, P. Guan, X. Wu, and Y.-C. Chen, "Lasing-encoded microsensor driven by interfacial cavity resonance energy transfer," Adv. Opt. Mater. **8**, 1901596 (2020).
25. A. Jonas, M. Aas, Y. Karadag, S. Manioglu, S. Anand, D. McGloin, H. Bayraktar, and A. Kiraz, "In vitro and in vivo biolasing of fluorescent proteins suspended in liquid microdroplet cavities," Lab Chip **14**, 3093–3100 (2014).
26. W. Lee, Q. Chen, X. Fan, and D. K. Yoon, "Digital DNA detection based on a compact optofluidic laser with ultra-low sample consumption," Lab Chip **16**, 4770–4776 (2016).
27. C. Gong, Y. Gong, X. Zhao, Y. Luo, Q. Chen, X. Tan, Y. Wu, X. Fan, G.-D. Peng, and Y.-J. Rao, "Distributed fibre optofluidic laser for chip-scale arrayed biochemical sensing," Lab Chip **18**, 2741–2748 (2018).
28. O. Erol, T. Pelin, A. Ozan, H. Ersin, and B. Mehmet, "Label-free biosensing with high selectivity in complex media using microtoroidal optical resonators," Sci. Rep. **5**, 13173 (2015).

29. S. Soria, F. Baldini, S. Berneschi, F. Cosi, A. Giannetti, G. N. Conti, S. Pelli, G. Righini, and B. Tiribilli, "High-Q polymer-coated microspheres for immunosensing applications," Opt. Express **17**, 14694–14699 (2009).

30. E. Kim, M. D. Baaske, and F. Vollmer, "*In situ* observation of single-molecule surface reactions from low to high affinities," Adv. Mater. **28**, 9941–9948 (2016).

31. Y. Chen, U. Schoeler, C. Huang, and F. Vollmer, "Combining whispering-gallery mode optical biosensors with microfluidics for real-time detection of protein secretion from living cells in complex media," Small **14**, 1703705 (2018).

32. H. H. Mai, T. T. Nguyen, K. M. Giang, X. T. Do, T. T. Nguyen, H. C. Hoang, and V. D. Ta, "Chicken albumen-based whispering gallery mode microlasers," Soft Matter **16**, 9069–9073 (2020).

33. A. Francois, N. Riesen, H. Ji, S. Afshar V., and T. M. Monro, "Polymer based whispering gallery mode laser for biosensing applications," Appl. Phys. Lett. **106**, 031104 (2015).

34. A. Capocefalo, E. Quintiero, M. Bianco, A. Zizzari, S. Gentilini, C. Conti, V. Arima, I. Viola, and N. Ghofraniha, "Random laser spectral fingerprinting of lithographed microstructures," Adv. Mater. Technol. **6**, 2001037 (2021).

35. A. Capocefalo, E. Quintiero, C. Conti, N. Ghofraniha, and I. Viola, "Droplet lasers for smart photonic labels," ACS Appl. Mater. Interfaces **13**, 51485–51494 (2021).

36. N. Ghofraniha, L. La Volpe, D. Van Opdenbosch, C. Zollfrank, and C. Conti, "Biomimetic random lasers with tunable spatial and temporal coherence," Adv. Opt. Mater. **4**, 1998–2003 (2016).

37. G. Righini, Y. Dumeige, P. Feron, M. Ferrari, G. N. Conti, D. Ristic, and S. Soria, "Whispering gallery mode microresonators: Fundamentals and applications," Riv. Nuovo Cim. **34**, 435–488 (2011).

38. A. Soloperto, D. Quaglio, P. Baiocco, I. Romeo, M. Mori, M. Ardini, C. Presutti, I. Sannino, S. Ghirga, A. Iazzetti, R. Ippoliti, G. Ruocco, B. Botta, F. Ghirga, S. Di Angelantonio, and A. Boffi, "Rational design and synthesis of a novel bodipy-based probe for selective imaging of tau tangles in human IPSC-derived cortical neurons," Sci. Rep. **12**, 5257 (2022).

39. A. Tavlove and S. Hagness, *Computational Electrodynamics: The Finite-Difference Time-Domain Method*, 3rd ed. (Artech House, 2000).

40. S. Gentilini, A. Fratalocchi, L. Angelani, G. Ruocco, and C. Conti, "Ultrashort pulse propagation and the Anderson localization," Opt. Lett. **34**, 130–132 (2009).

41. S. Gentilini and C. Conti, "Optomechanics of random media," Phys. Rev. A **91**, 043813 (2015).

42. D. W. Walker and J. J. Dongarra, "MPI: a standard message passing interface," Supercomputer **12**, 56 (1996).

43. Y. W. Jun, S. W. Cho, J. Jung, Y. Huh, Y. Kim, D. Kim, and K. H. Ahn, "Frontiers in probing Alzheimer's disease biomarkers with fluorescent small molecules," ACS Cent. Sci. **5**, 209–217 (2019).

44. M. Baaske, M. Foreman, and F. Vollmer, "Single-molecule nucleic acid interactions monitored on a label-free microcavity biosensor platform," Nat. Nanotechnol. **9**, 933–939 (2014).

45. F. Saglimbeni, S. Bianchi, G. Bolognesi, G. Paradossi, and R. Di Leonardo, "Optical characterization of an individual polymer-shelled microbubble structure via digital holography," Soft Matter **8**, 8822–8825 (2012).

46. S. Armstrong, Jr., M. Budka, K. Morrison, and M. Hasson, "Preparation and properties of serum and plasma proteins. XII. The refractive properties of the proteins of human plasma and certain purified fractions," J. Am. Chem. Soc. **69**, 1747–1753 (1947).

47. G. L. Long and J. D. Winefordner, "Limit of detection. A closer look at the IUPAC definition," Anal. Chem. **55**, 712A–724A (1983).

48. S. Subramanian, H. B. Jones, S. Frustaci, S. Winter, M. W. van der Kamp, V. L. Arcus, C. R. Pudney, and F. Vollmer, "Sensing enzyme activation heat capacity at the single-molecule level using gold-nanorod-based optical whispering gallery modes," ACS Appl. Nano Mater. **4**, 4576–4583 (2021).

49. S. Shopova, R. Rajmangal, S. Holler, and S. Arnold, "Plasmonic enhancement of a whispering-gallery-mode biosensor for single nano-particle detection," Appl. Phys. Lett. **98**, 243104 (2011).

50. T. L. McMeekin, M. L. Groves, and N. J. Hipp, *Refractive Indices of Amino Acids, Proteins, and Related Substances* (ACS Publications, 1964), chap. 4, pp. 54–66.